Diffusion calculations on reconstructed bentonite microstructures with anion exclusion effects

Fatiha Bouchelaghem

Diffusion calculations on reconstructed bentonite microstructures with anion exclusion effects

Fatiha Bouchelaghem[1*]

[1*]Institut Jean Le Rond d'Alembert, Sorbonne Universite, 4 Place Jussieu, Paris, 75005, France.

Corresponding author(s). E-mail(s): fatiha.bouchelaghem@sorbonne-universite.fr;

Abstract

Due to their prevalence in the lithosphere and their high capability of sorbing pollutants, smectite clays play a foreground role in environmental pollution studies, waste management and soil science. In complementarity with existing approaches at the molecular or macroscopic scales, real microstructures have been employed to investigate ionic transport by diffusion through montmorillonite and water-saturated Wyoming bentonite at intermediate scales ranging between the nanometer and the micrometer. The coupled solute transport and electrostatic phenomena investigated at the nanopore scale are upscaled using the Homogenization of Porous Media approach. Homogenization computations rely on a hierarchical description of bentonite that acknowledges the existence of pores networks at different scales. At the scale of montmorillonite layers, digitized TEM images have been employed to simulate diffusion of ionic solutes by considering electrostatic interactions in the vicinity of the negatively-charged clay platelets' surface. Finite Element microstructures are created after extraction of the contours of the layers using dedicated image processing algorithms. Local electric potential distribution, anion exclusion and cation inclusion are displayed by ion distribution maps. The effective diffusion tensor and the transport equation obtained through volume averaging are then used to simulate diffusion at the scale of a Wyoming bentonite sample composed of clay gels of variable density, solid grains and micropores. Qualitative comparisons were made with existing diffusion data, and a particular attention is given to the anisotropy of the diffusion tensors at both the mesoscopic

and macroscopic scales.
keywords: Ionic diffusion, Anion exclusion, Montmorillonite, Compacted Saturated Bentonite, Digitized TEM microstructures, Numerical Homogenization, Finite Element computations, Anisotropy.

1 Introduction

Due to their prevalence in the lithosphere and their high capability of sorbing pollutants, smectite clays play a foreground role in environmental pollution studies, waste management and soil science (Choi and Oscarson, 1996; Gonzales Sanchez et al., 2009; Suuronen et al., 2014; Whittaker et al., 2020). The use of compacted bentonite as a buffer material in radioactive or domestic waste storage is indeed motivated by its exceptional swelling and retention properties. At the nanoscopic scale, their microstructure is characterized by a regular stacking of montmorillonite layers of very high aspect ratio, with a permanent negative surface charge compensated by interlayer cations. The resulting arrangement will condition the microstructural properties (cationic exchange capacity, specific surface, swelling potential, retention of water and pollutants), and the resulting hydro-mechanical behavior of hydrated smectites at engineering scale (Hetzel et al., 1994; Pusch, 2001; Smith et al., 2004; Whittaker et al., 2020).

Diffusive transport is the predominant mechanism of solute transport through saturated and compacted smectite clays subjected to natural hydraulic gradients (Gonzales Sanchez et al., 2009). As a result, there is a large experimental database related to diffusion of water and charged solutes through water-saturated bentonite, on a wide range of spatial and temporal scales (Choi and Oscarson, 1996; Glaus et al., 2007; Gonzales Sanchez et al., 2009; Kemper and van Schaik, 1966; Kozaki et al., 2001; Malikova et al., 2008; Marry and Turq, 2003; Nakashima, 2003; Sato and Suzuki, 2003; Sato, 2005; Smith et al., 2004; Suzuki et al., 2004).
Diffusion measurements at the nanoscopic scale (Gonzales Sanchez et al., 2009) have shown the preponderance of surface effects, such as reduced water viscosity and electrostatic interactions between the diffusing species (water molecules, ions) and the clay surfaces and compensating cations, those effects being expressed by an electrostatic constraint factor. At the micrometer scale, the morphology and the connectivity of the pore network play a foreground role in the resulting diffusion through micropores, this contribution being expressed by an overall geometric factor or tortuosity. However, as pointed out in (Gonzales Sanchez et al., 2009), those factors cannot be related to the porosity or other easily derived properties of the porous medium, and must be regarded as empirical parameters. Monte Carlo and Molecular Dynamics (MD) simulations have been employed in order to identify the interlayer molecular structure and local diffusion coefficients of tracers in the vicinity

of charged montmorillonite mineral surfaces (Chang et al., 1995; Marry and Turq, 2003; Tournassat et al., 2016). The simulated values are then introduced into a macroscopic model of diffusion using the known porosity value and empirical parameters such as the constrictivity factor and tortuosity. Recently, (Tournassat et al., 2016) employed MD simulations in order to investigate anion exclusion from very narrow nanopores (of widths lower than 1.5 nm). Three individual clay mineral layers, and three nanopores in contact with a larger mesopore are represented, all the layers being parallel and displaying a straight and rigid structure throughout the simulations. Detailed concentration profiles are obtained in the interlayer pores and in the mesopores. A recent model of ionic diffusion transport by (Bacle et al., 2016) is based on Brownian dynamics simulations, and offers an elaborate description of the microstructure by stacks of overlapping cylindrical clay platelets, but no electrostatic effects are taken into account. To conclude, although the resulting macroscopic diffusion coefficients are close to experimental data, Monte Carlo and Molecular Dynamics Simulations cannot take into account the geometry of compacted clays beyond the interlayer region (Marry and Turq, 2003). One drawback of MD simulations lies also in the fact that the simulated clay region is too limited in space to take into account interlayer pores and micropores that are not influenced by the montmorillonite layers' surfaces, and which are also encountered in clay-water mixtures. Besides, as pointed out in (Pusch, 2001), most of the microstructural models of clays refer only to the detailed particle-to-particle interaction by assuming a parallel arrangement for two or three montmorillonite layers, and disregard the real pore distribution and the scale-dependent variation in density of the clay gels.
(Wu et al., 2020) have performed pore scale simulations of radionuclide tracer diffusion in compacted montmorillonite using generated three-dimensional microstructures and the Lattice Boltzmann Method. Their investigation notably shows the influence of surface charge and the interaction of overlapping electrical double layers on anion exclusion, in agreement with experimental data. However, the model requires extensive numerical resources to generate the microstructures based on a limited set of pore characteristics (such as porosity, surface area and mean pore size) with no independent means of checking the representativity of those microstructures, and the computations do not allow to express the diffusion tensor at the mesoscopic scale.

In complementarity with recent works, we try to model ionic diffusion using a realistic description of the hierarchical nature of smectite microstructure. We aim to investigate the specific contributions of the surface charge and the interlayer porosity at the nanoscopic scale, as well as the part played by micropores and clay gels of varying density at the micrometer scale. More specifically, we aim to develop a better understanding of the role played by the inherent flexibility of negatively charged montmorillonite layers and their natural arrangement in more or less parallel stackings at the nanoscopic scale (Honorio

et al., 2018), during ionic transport by diffusion characterized by cation inclusion and anion exclusion. For this reason, we consider a real microstructure composed of a sufficient number of long and thin elementary layers, in order to account for the relatively ordered and laminated structure of montmorillonites. During the model development, we use a rigorous and sequential approach in order to acknowledge the hierarchical organization of porous spaces in natural bentonites while avoiding the introduction of empirical fitting parameters. The Homogenization of Periodic Media approach is employed to obtain the effective properties governing solute transport by diffusion at the scale of an assembly of montmorillonite layers and interlayer water. Three levels of description are considered during the model derivation through homogenization. The microscopic level designates the scale of stacked flexible montmorillonite lamellae and interlayer water whose physical properties are affected by the pore walls (Marry and Turq, 2003; Cheng and Hendry, 2014). The mesoscopic level refers to the scale of clay gels, solid grains and inter-aggregate pores (Keller et al., 2014; Nakashima, 2003; Tomioka et al., 2010). The effective properties computed by upscaling from the microscopic to the mesoscopic scales are affected to the clay gels, while diffusion within the inter-aggregate micropores is assumed to take place without surface effects. The macroscopic level corresponds to samples subjected to diffusion tests in the laboratory. Upscaling is then performed from the mesoscopic scale to the scale of a laboratory sample of bentonite to compute the macroscopic diffusion tensor and the effective coupling tensor (originating from the negatively charged montmorillonite layers) of bentonite. The overall diffusion behavior of bentonite at the engineering scale is naturally expected to depend on the corresponding processes taking place at lower scales within interlayer nanopores and micropores, and tackling both scales simultaneously remains elusive. The advantage of the proposed approach based on asymptotic analysis is that the nanoscopic and mesoscopic scales can be studied separately by considering the relevant geometries and physical processes at each scale, while the coupling coefficients derived through upscaling (or averaging) can be identified by solving simple elementary problems.

2 Construction of the numerical microstructures

2.1 At the microscopic scale

The microstructure illustrated in Figure 1 has been obtained by exploiting a high-resolution Transmission Electron Micrograph from (Hetzel et al., 1994), and represents one quarter of the complete Representative Volume Element (see Section 3.4). The porous medium investigated at the nanoscale is composed of two phases: the solid phase of montmorillonite layers Ω_s and the interstitial space saturated with the electrolyte solution Ω_f. Ω_s and Ω_f are expressed in m^3 and we consider a length L_z in the direction perpendicular to

the plane of the Figure such that $L_z \gg l'$ and $L_z = \mathcal{O}(l)$, with l' the characteristic size of the heterogeneities present within the microstructure, while l is the characteristic size of a stacking of montmorillonite layers (see Section 3.2, $l' =$ 3-4 nm represents the interlayer distance, and $l = 0.4$ μm in Figure 1). Consequently, solute transport is considered to be invariant in the direction of L_z, and we can restrict the study to a two-dimensional cross-section of the montmorillonite clay gels, such as represented in Figure 1. Using two-dimensional microstructures for describing solute transport around montmorillonite layers is justified by typical lateral extensions L_z observed for montmorillonite surfaces, which are more than a hundred times higher than their average thickness (Honorio et al., 2018; Malikova et al., 2008; Pusch, 2001), as well as by experimental evidence (Gonzales Sanchez et al., 2009; Malikova et al., 2008; Marry and Turq, 2003).

The porosity of the microstructure represented in Figure 1 is equal to 82.2 %, and is close to the value of 87 % employed by (Smith et al., 2004) in their numerical study, and to experimental values of porosity (comprised between 76 % and 90 %) reported in (Smith et al., 2004) for pure montmorillonite. The

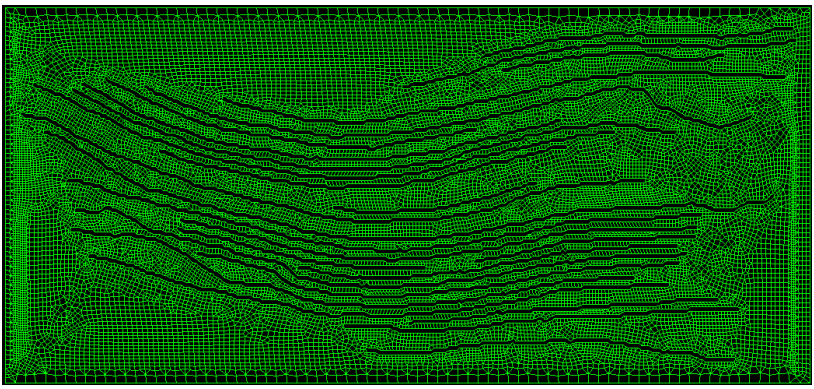

Fig. 1 Finite Element Microstructure obtained after processing of a Transmission Electron Micrograph from (Hetzel et al, 1994). Image width:0.4 μm.

image analysis procedure developed using MATLAB is the result of trial and error. Each grayscale TEM image is thresholded first to obtain a binary image, without prior filtering. The threshold value is found based on the histogram of the image, and the choice is confirmed by visual inspection. Besides, it has been observed that a single threshold value leads generally to better final results than an adaptive thresholding. Contrast enhancement is then performed by bottom-hat and top-hat filtering. Next, a series of morphological opening and closing operations are performed with elongated elements of increasing size, oriented along the average orientation computed for the assembly of layers. Objects displaying an eccentricity smaller than the average eccentricity are then removed, as well as objects which area represents less than one percent of the maximal object area. Finally, the contours of the remaining objects

are extracted using Moore-Neighbor's algorithm with Jacob's stopping criterion (Gonzalez et al., 2004). A dedicated procedure has been implemented to import the coordinates of the contour points and create the microstructure in the Finite Element-based code Castem (Le Fichoux, 2022).

2.2 At the mesoscopic scale

Numerical microstructures have been obtained at the mesoscopic scale by processing micrographs taken by Transmission Electron Microscopy (TEM) on resin-impregnated samples of Wyoming bentonite (Pusch, 2001). Four distinct phases are considered in the original TEM micrographs: solid grains, dense clay gels, soft clay gels, and micropores. The solid grains refer to the non-smectite phases (quartz, feldspars, mica and chlorite) and the smectite grains which have not been hydrated. This microstructure has been retained as clay gels are spontaneously formed through hydration and expansion of aggregates that exfoliate from the grains exposed to water, while according to (Pusch, 2001) comparative studies with similar bentonites examined using High Voltage Electron Microscopy have shown that microstructural features (such as void size and clay density) are preserved by acrylate embedment.

The thresholding procedure is based on the algorithm of maximization of the gray level histogram's entropy developed by (Kapur et al., 1985). The threshold values obtained are validated by comparison of the resulting phase proportions with the cumulative distribution curve and the initial known phase proportions (Bouchelaghem and Pusch, 2017; Tomioka et al., 2010). The contours are extracted separately for each phase using Moore-Neighbor's algorithm with Jacob's stopping criterion, before being imported and used to create the Finite Element mesh in Castem. Such a microstructure is illustrated in Figure 6. The resolution is about 25 nanometers per pixel, which allows a good representation of the internal microstructure.

3 Homogenization at the microscopic scale

3.1 Modeling assumptions and local description of the problem

The modeling work starts with equations that have classically been employed to generalize Fick's model of diffusion, in order to account for chemical and electrostatic couplings when ionic species are transported within a charged porous medium (Cheng and Hendry, 2014; Moyne and Murad, 2006; Smith et al., 2004). The molar flux density is expressed by Nernst-Planck equation in the stationary mass balance equation written for each chemical species i of concentration c_i and valence z_i (Gross and Osterle, 1968; Morrison and

Osterle, 1965):

$$\nabla_x \cdot \left(D_{0,i} \nabla_x c_i + D_{0,i} \frac{F}{RT} c_i z_i \nabla_x \psi \right) = 0 \text{ in } \Omega_\mathrm{f} \tag{1}$$

In Eq. (1), $D_{0,i}$ is the self-diffusion coefficient of solute i in the pore fluid, F is Faraday's constant, R the universal gas constant and T the constant absolute temperature. $\nabla_x = \sum_{i=1}^{2} \frac{\partial}{\partial x_i} \mathbf{e}_i$ is the nabla operator of differentiation with respect to the Cartesian spatial coordinates.

Poisson's equation with a source term representing the net charge density (Cheng and Hendry, 2014; Moyne and Murad, 2006) for N solutes is written to describe the distribution of the electric potential ψ under steady-state conditions:

$$\nabla_x \cdot (\tilde{\epsilon} \nabla_x \psi) = -F \sum_{i=1}^{N} z_i c_i \text{ in } \Omega_\mathrm{f} \tag{2}$$

where the permittivity $\tilde{\epsilon}$ is the product of the permittivity of vacuum ϵ_0 and the relative permittivity of water ϵ_w: $\tilde{\epsilon} = \epsilon_0 \, \epsilon_w$.

Eqns. (1) and (2) are completed with boundary conditions in the vicinity of the montmorillonite platelets' surface Γ:

$$D_{0,i} \left(\nabla_x c_i + \frac{F}{RT} c_i z_i \nabla_x \psi \right) \cdot \mathbf{n} = 0 \text{ on } \Gamma \tag{3}$$

$\mathbf{n}$, the normal unit vector on Γ, points towards Ω_s.

The voltage gradient flux is imposed at the surface of the montmorillonite layers in order to express the relationship between ψ and the known surface charge density σ (Cheng and Hendry, 2014; Liu et al., 2019):

$$\tilde{\epsilon} \nabla_x \psi \cdot \mathbf{n} = -\sigma \text{ on } \Gamma \tag{4}$$

In what follows, to simplify the model presentation, we consider a binary solution ($c_i = c^+$, $z_i = z^+$ and $D_{0,i} = D^+$ for cations; $c_i = c^-$, $z_i = -z^-$ and $D_{0,i} = D^-$ for anions):

$$F \sum_{i=1}^{N} z_i c_i = F \left(z^+ c^+ - z^- c^- \right) \tag{5}$$

Following (Cheng and Hendry, 2014; Moyne and Murad, 2006; Sasidhar and Ruckenstein, 2003), the electric potential ψ is decomposed into two components:

$$\psi = \psi_\mathrm{ex} + \psi_\mathrm{in} \tag{6}$$

where ψ_ex is associated with the exterior solution and the induced membrane potential, while ψ_in is related with the interior diffuse double-layer (DDL) and

the negative charge on the montmorillonite layers. ψ_{in} is effective within the Debye length, so that within the DDL, the concentration of cations is dominant relative to the concentration of anions, but both tend to approach their respective equilibrium concentrations in the exterior solution. This implies a Boltzmann distribution of concentration for cations (c^+) and anions (c^-) (see (Gross and Osterle, 1968; Morrison and Osterle, 1965) for a detailed derivation of the following expression):

$$c^{\pm} = c^{\pm}_{\text{ex}} \exp\left(\mp \frac{F z^{\pm} \psi_{\text{in}}}{RT}\right) \tag{7}$$

with $c^{\pm}_{\text{ex}}$ the electrolyte concentration associated with the exterior solution. As a result, Eqn. (2) can be decomposed in two equations:

$$\begin{aligned} \nabla_x \cdot (\tilde{\epsilon}\, \nabla_x \psi_{\text{ex}}) &= 0 \\ \nabla_x \cdot (\tilde{\epsilon}\, \nabla_x \psi_{\text{in}}) &= -F \left(z^+ c^+_{\text{ex}} \exp\left(-\frac{F z^+ \psi_{\text{in}}}{RT}\right) - z^- c^-_{\text{ex}} \exp\left(\frac{F z^- \psi_{\text{in}}}{RT}\right) \right) \end{aligned} \tag{8}$$

3.2 Scaling analysis

To normalize the equations, proper estimates of the physical variables are required. The subscript c is used to denote a characteristic value, such that each quantity f ($f = c^+, c^-, \psi, ...$) is written as: $f = f_c\, f'$, with f' the corresponding dimensionless variable.
Following an approach detailed in (Sanchez-Palencia, 1980), two characteristic lengths scales are introduced:
- a microscopic length l' associated with heterogeneities present within the microstructure. As in (Cheng and Hendry, 2014; Moyne and Murad, 2006), we take l' as the Debye length τ_{D}:

$$l' = \tau_{\text{D}} = \sqrt{\frac{\epsilon_0 \epsilon_w\, R\, T}{F^2 c_c}} \tag{9}$$

τ_{D} represents the scale of variation of the electric potential ψ or the thickness of the double-layer. τ_{D}, which depends on the electrolyte concentration $c_c = (c^{\pm}_{\text{ex}})_c$ (typical values being comprised between 1 and 100 mol $\cdot$ m^{-3} (Liu et al., 2019; Whittaker et al., 2020)), varies generally between one and ten nanometers.
- a mesoscopic length l associated with typical dimensions of the microstructure (i.e. the characteristic dimension of a montmorillonite particle, several hundreds of nanometers).

The perturbation parameter ε' is then defined by the following ratio: $\varepsilon' = \frac{l'}{l}$, such that $\varepsilon' \ll 1$ guarantees the separation of scales required for homogenization (Sanchez-Palencia, 1980).

Physical constants are readily estimated (Cheng and Hendry, 2014; Gross and Osterle, 1968; Morrison and Osterle, 1965; Smith et al., 2004):
$F_c = F = 96485\ \mathrm{C \cdot mol^{-1}}$, $R_c = R = 8.3145\ \mathrm{J \cdot K^{-1} \cdot mol^{-1}}$, $T_c = T = 293\ \mathrm{K}$, $\tilde{\epsilon}_c = \tilde{\epsilon} = \epsilon_0 \epsilon_w = 8.8542 \times 10^{-12} \times 78 = 6.903 \times 10^{-10}\ \mathrm{C^2 \cdot J^{-1} \cdot m^{-1}}$.
As in (Cheng and Hendry, 2014; Gross and Osterle, 1968; Liu et al., 2019; Smith et al., 2004; Moyne and Murad, 2006), we set $\psi_c = \frac{RT}{F}$. The characteristic length is defined as $l_c = l'$. From Eqn. (2) the characteristic value for the electrolyte concentration is taken to be $c_c = \frac{\tilde{\epsilon}\psi_c}{Fl'^2}\ \mathrm{mol \cdot m^{-3}}$, while from Eqn. (4) $\sigma_c = \frac{\tilde{\epsilon}\psi_c}{l'} = \mathcal{O}(0.05)\ \mathrm{C \cdot m^{-2}}$ (Cheng and Hendry, 2014; Liu et al., 2019; Moyne and Murad, 2006).

The dimensionless space variable $x'_i = \frac{x_i}{l}$ ($i = 1, 2$ in 2D) is introduced, together with the dimensionless volumes $\Omega'_\mathrm{f} = \frac{\Omega_\mathrm{f}}{l^2 L_z}$, $\Omega'_\mathrm{s} = \frac{\Omega_\mathrm{s}}{l^2 L_z}$. Ω' represents the volume of the complete microstructure composed of interstitial spaces and montmorillonite layers: $\Omega' = \Omega'_\mathrm{f} + \Omega'_\mathrm{s}$. Γ' designates the interface between the montmorillonite platelets Ω'_s and the interstitial space Ω'_f within Ω'. Using the previous estimates of c_c, ψ_c and σ_c and accounting for Eqn.(7), the system of Eqs.(1),(3),(4) and (8) is rewritten in dimensionless form as follows:

$$\nabla_{x'} \cdot \left(D'^{+} \exp\left(-z^{+}\psi'_\mathrm{in}\right) \left(\nabla_{x'} c'^{+}_\mathrm{ex} + z^{+} c'^{+}_\mathrm{ex} \nabla_{x'} \psi'_\mathrm{ex} \right) \right) = 0 \text{ in } \Omega'_\mathrm{f} \tag{10}$$

$$\nabla_{x'} \cdot \left(D'^{-} \exp\left(z^{-}\psi'_\mathrm{in}\right) \left(\nabla_{x'} c'^{-}_\mathrm{ex} - z^{-} c'^{-}_\mathrm{ex} \nabla_{x'} \psi'_\mathrm{ex} \right) \right) = 0 \text{ in } \Omega'_\mathrm{f} \tag{11}$$

$$\Delta_{x'} \psi'_\mathrm{ex} = 0 \text{ in } \Omega'_\mathrm{f} \tag{12}$$

$$\varepsilon'^2 \Delta_{x'} \psi'_\mathrm{in} = -\left(z^{+} c'^{+}_\mathrm{ex} \exp\left(-z^{+}\psi'_\mathrm{in}\right) - z^{-} c'^{-}_\mathrm{ex} \exp\left(z^{-}\psi'_\mathrm{in}\right) \right) \text{ in } \Omega'_\mathrm{f} \tag{13}$$

$$D'^{+} \exp\left(-z^{+}\psi'_\mathrm{in}\right) \left(\nabla_{x'} c'^{+}_\mathrm{ex} + z^{+} c'^{+}_\mathrm{ex} \nabla_{x'} \psi'_\mathrm{ex} \right) \cdot \mathbf{n} = 0 \text{ on } \Gamma' \tag{14}$$

$$D'^{-} \exp\left(z^{-}\psi'_\mathrm{in}\right) \left(\nabla_{x'} c'^{-}_\mathrm{ex} - z^{-} c'^{-}_\mathrm{ex} \nabla_{x'} \psi'_\mathrm{ex} \right) \cdot \mathbf{n} = 0 \text{ on } \Gamma' \tag{15}$$

$$\nabla_{x'} \psi'_\mathrm{ex} \cdot \mathbf{n} = 0 \text{ on } \Gamma' \tag{16}$$

$$\varepsilon' \nabla_{x'} \psi'_\mathrm{in} \cdot \mathbf{n} = -\sigma' \text{ on } \Gamma' \tag{17}$$

By assuming a local periodicity for the microstructure and all physical variables, c^{+}_ex, c^{-}_ex, ψ_in and ψ_ex can be written as asymptotic developments with respect to the mesoscopic coordinates $x' = \frac{x}{l}$ and the local (microscopic) coordinates $y' = \frac{x}{l'} = \frac{x'}{\varepsilon'}$ (to simplify the notation, in the following we drop the $'$ symbol in the expression of dimensionless quantities):

$$c^{+}_\mathrm{ex}(x,y) = c^{+(0)}_\mathrm{ex}(x,y) + \varepsilon'\, c^{+(1)}_\mathrm{ex}(x,y) + \varepsilon'^2\, c^{+(2)}_\mathrm{ex}(x,y) + \ldots \tag{18}$$

$$c^{-}_\mathrm{ex}(x,y) = c^{-(0)}_\mathrm{ex}(x,y) + \varepsilon'\, c^{-(1)}_\mathrm{ex}(x,y) + \varepsilon'^2\, c^{-(2)}_\mathrm{ex}(x,y) + \ldots \tag{19}$$

$$\psi_\mathrm{in}(x,y) = \psi^{(0)}_\mathrm{in}(x,y) + \varepsilon'\, \psi^{(1)}_\mathrm{in}(x,y) + \varepsilon'^2\, \psi^{(2)}_\mathrm{in}(x,y) + \ldots \tag{20}$$

$$\psi_\mathrm{ex}(x,y) = \psi^{(0)}_\mathrm{ex}(x,y) + \varepsilon'\, \psi^{(1)}_\mathrm{ex}(x,y) + \varepsilon'^2\, \psi^{(2)}_\mathrm{ex}(x,y) + \ldots \tag{21}$$

where each term $f^{(i)}(x,y)$ in the developments above is Ω'-periodical.

As a result, differentiation with respect to x, ∇_x, is replaced by differentiation with respect to x and y, $\nabla_x + \frac{1}{\varepsilon'}\nabla_y$ (Bouchelaghem, 2018;

Sanchez-Palencia, 1980). Substituting asymptotic developments (18)-(21) into Eqns.(10)-(17) and accounting for the new rules of differentiation, local boundary-value problems are then derived at successive orders of approximation with respect to ε'. The local problems allow to identify the mesoscopic quantities (that depend only on x) and the local distributions of concentration and electric potential, as well as to obtain the effective properties by averaging over the RVE.

3.3 Local problems

At the lowest level, it is straightforward to show that $c_{\text{ex}}^{+(0)}$, $c_{\text{ex}}^{-(0)}$ and $\psi_{\text{ex}}^{(0)}$ are mesoscopic quantities, which do not depend on the local variable y (see Appendix B). This allows to identify $\frac{\partial c_{\text{ex}}^{+(0)}(x)}{\partial x_i}$ and $\frac{\partial c_{\text{ex}}^{-(0)}(x)}{\partial x_i}$ $(i = 1, 2)$ as the mesoscopic force components of the imposed electrolyte concentration gradient, and $\frac{\partial \psi_{\text{ex}}^{(0)}(x)}{\partial x_i}$ as the mesoscopic force of the induced membrane potential gradient (Cheng and Hendry, 2014). The previous results have important implications concerning the resolution of the local problems, which will be greatly simplified in comparison with the original coupled system of Nernst-Planck and Poisson-Boltzmann equations Eqs. (1) to (4) written for the ionic concentrations c_i and electric potential ψ. One of the strengths of the asymptotic analysis is that it enables to identify the physical quantities that don't depend on the local space variable y, and therefore to obtain a series of (mostly) uncoupled local problems.

If we consider Eq. (13) at order $\mathcal{O}(\varepsilon'^0) = \mathcal{O}(1)$ and Eq. (17) at order $\mathcal{O}(1)$, $\psi_{\text{in}}^{(0)}$ verifies the following dimensionless problem within the unit cell Ω':

$$\Delta_y \psi_{\text{in}}^{(0)} = -z^+ c_{\text{ex}}^{+(0)} \exp\left(-z^+ \psi_{\text{in}}^{(0)}\right) + z^- c_{\text{ex}}^{-(0)} \exp\left(z^- \psi_{\text{in}}^{(0)}\right) \text{ in } \Omega'_{\text{f}}$$

$$\begin{gathered} \nabla_y \psi_{\text{in}}^{(0)} \cdot \mathbf{n} = -\sigma \text{ on } \Gamma' \\ \psi_{\text{in}}^{(0)} \ \Omega' - \text{periodical} \\ \langle \psi_{\text{in}}^{(0)} \rangle = \frac{1}{|\Omega'|} \int_{\Omega'_{\text{f}}} \psi_{\text{in}}^{(0)} dV = 0 \end{gathered} \tag{22}$$

At the next order of approximation, we obtain the problems verified by $\psi_{\text{ex}}^{(1)}$, $c_{\text{ex}}^{+(1)}$ and $c_{\text{ex}}^{-(1)}$ (see Appendix B). Contrary to the results presented in (Cheng and Hendry, 2014), it appears that $\psi_{\text{ex}}^{(1)}$ is not constant within the interlayer pores, and varies within the microstructure under the action of the induced mesoscopic potential gradient $\nabla_x \psi_{\text{ex}}^{(0)}$ on the montmorillonite layers' surface (we use Einstein summation convention on repeated indices):

$$\psi_{\text{ex}}^{(1)}(x, y) = \beta_l(y) \frac{\partial \psi_{\text{ex}}^{(0)}}{\partial x_l}(x) = \boldsymbol{\beta}(y) \cdot \nabla_x \psi_{\text{ex}}^{(0)} \tag{23}$$

The local problem verified by $\beta_l(y)$, $l = 1, 2$, given by the set of Eqs.(B2) to (B5), is detailed in Appendix B.

After some developments (see Appendix B), we find that $c_{\text{ex}}^{+(1)}$ and $c_{\text{ex}}^{-(1)}$ depend linearly on the electrolyte concentration gradient $\nabla_x c_{\text{ex}}^{+(0)}$ and the membrane potential gradient $\nabla_x \psi_{\text{ex}}^{+(0)}$:

$$c_{\text{ex}}^{+(1)}(x,y) = c_l^+(y)\,\frac{\partial c_{\text{ex}}^{+(0)}}{\partial x_l}(x) + d_l^+(y)\,z^+ c_{\text{ex}}^{+(0)}\,\frac{\partial \psi_{\text{ex}}^{(0)}}{\partial x_l}(x) \tag{24}$$

$$c_{\text{ex}}^{-(1)}(x,y) = c_l^-(y)\,\frac{\partial c_{\text{ex}}^{-(0)}}{\partial x_l}(x) - d_l^-(y)\,z^- c_{\text{ex}}^{-(0)}\,\frac{\partial \psi_{\text{ex}}^{(0)}}{\partial x_l}(x) \tag{25}$$

c_l^+ and c_l^- $(l = 1, 2)$ verify the local problem given by Eqs. (B12) detailed in Appendix B.
d_l^+ and d_l^- $(l = 1, 2)$ verify the local problem given by Eqs. (B13) detailed in Appendix B.

By writing Eqs. (10) and (11) at order $\mathcal{O}((\varepsilon')^0) = \mathcal{O}(1)$ and averaging over the RVE, it is possible to obtain transport equations for $c_{\text{ex}}^{+(0)}$ and $c_{\text{ex}}^{-(0)}$ at the mesoscopic scale of clay gels in the following forms (see Appendix C):

$$\nabla_x \left(\mathcal{D}^{\pm} \cdot \nabla_x c_{\text{ex}}^{\pm\,(0)} \right) + \nabla_x \left(c_{\text{ex}}^{\pm\,(0)} \mathcal{D}_{\psi}^{\pm} \cdot \nabla_x \psi_{\text{ex}}^{(0)} \right) = 0 \tag{26}$$

In Eqs.(26), the components of the mesoscopic diffusion tensors $\mathcal{D}^{\pm}$ and the tensors $\mathcal{D}_{\psi}^{\pm}$ expressing the effect on ion diffusion of the membrane potential are defined as follows $(i, l = 1, 2)$:

$$\mathcal{D}_{il}^{\pm} = \frac{1}{|\Omega'|} \int_{\Omega'_{\text{f}}} \left(D^{\pm} \exp\left(\mp z^{\pm} \psi_{\text{in}}^{(0)}\right) \left(\frac{\partial c_l^{\pm}}{\partial y_i} + \delta_{il} \right) \right) dV \tag{27}$$

$$(\mathcal{D}_{\psi}^{\pm})_{il} = \frac{1}{|\Omega'|} \int_{\Omega'_{\text{f}}} \left(D^{\pm} \exp\left(\mp z^{\pm} \psi_{\text{in}}^{(0)}\right) z^{\pm} \left(\frac{\partial d_l^{\pm}}{\partial y_i} + \frac{\partial \beta_l}{\partial y_i} + \delta_{il} \right) \right) dV \tag{28}$$

3.4 Numerical Resolution with the Finite Element Method

On the outer boundary of the microstructure the ionic concentrations c_i and electric potential ψ are assumed to be periodical. Using symmetry considerations, the periodicity boundary conditions are transformed into more classical Dirichlet and Neumann boundary conditions. We assume that the domain occupied by the montmorillonite layers is symmetrical with respect to the coordinate axes and the origin of the coordinate system is a center of symmetry. As a result, the computations are performed on a quarter of the 2D microstructure.

The model is implemented in the Finite Element-based software Castem 2023 (Le Fichoux, 2022). Castem has been initially developed for the analysis of structures by the Finite Element Method and the modelling of thermo-hydro-mechanical behavior of a large variety of materials. Castem is based on an object-oriented approach, and requires the user to define its own sequence of instructions and procedures using the Gibiane language, in order to construct the geometry, the Finite Element Mesh, the boundary conditions, the rigidity matrix and the nonlinear resolution procedure. The choice of Castem has been motivated by its capacity to treat complex geometries starting from the coordinates of the points which constitute the montmorillonite layers' surfaces (obtained using MATLAB and imported in Castem), to define a large variety of boundary conditions, and to customize the resolution procedure for nonlinear problems (control of the local iterations steps, update of the nonlinear coefficients, convergence criterion ...). We refer to its website (https://www-cast3m.cea.fr/index.php) for an extensive documentation (in French) and an overview of its capabilities ranging from structural mechanics to fluid mechanics.

4 Results and Discussion

For the sake of simplicity, as in (Cheng and Hendry, 2014; Smith et al., 2004), a single binary monovalent salt (NaCl), completely dissolved in water, is considered, such that $z^+ = z^- = 1$ and $c_{\text{ex}}^{+(0)} = c_{\text{ex}}^{-(0)} = c_{\text{ex}}^{(0)}$.

4.1 Electric potential and Ion concentration maps

Figure 2 displays the electric potential $\psi_{\text{in}}^{(0)}$ in V, obtained at the first order of approximation by solving the system of Eqs. (22), and the osmotic pressure $p_{\text{in}}^{(0)}$ in Pa computed using the microstructure illustrated in Figure 1. The swelling or osmotic pressure that develops within the interlayer pores can be expressed as a function of the first order approximation of ion concentrations (Cheng and Hendry, 2014) (in the following expressions of the osmotic pressure and ionic concentrations $\psi_{\text{in}}^{(0)}$ represents the physical electric potential and is expressed in V):

$$p_{\text{in}}^{(0)} = RT\left((\exp(-\frac{F\,z^+\psi_{\text{in}}^{(0)}}{RT}) - 1)c_{\text{ex}}^{+(0)} + (\exp(\frac{F\,z^-\psi_{\text{in}}^{(0)}}{RT}) - 1)c_{\text{ex}}^{-(0)}\right) \quad (29)$$

Neumann boundary condition in Eqs. (22) applied on Γ' constitutes the main source term for $\psi_{\text{in}}^{(0)}$, as attested by higher isovalues in the vicinity of Γ. However, through the source term in Eq. (3.3), the membrane potential depends also strongly on each ion concentration $c_{\text{ex}}^{\pm(0)}$ weighted by its valence $z^{\pm}$. As a result, the spatial distribution of cations and anions in interlayer pores, and the effective diffusion tensor will be affected by the external salt concentration, as has been experimentally observed in Glaus et al. (2007) for more compacted

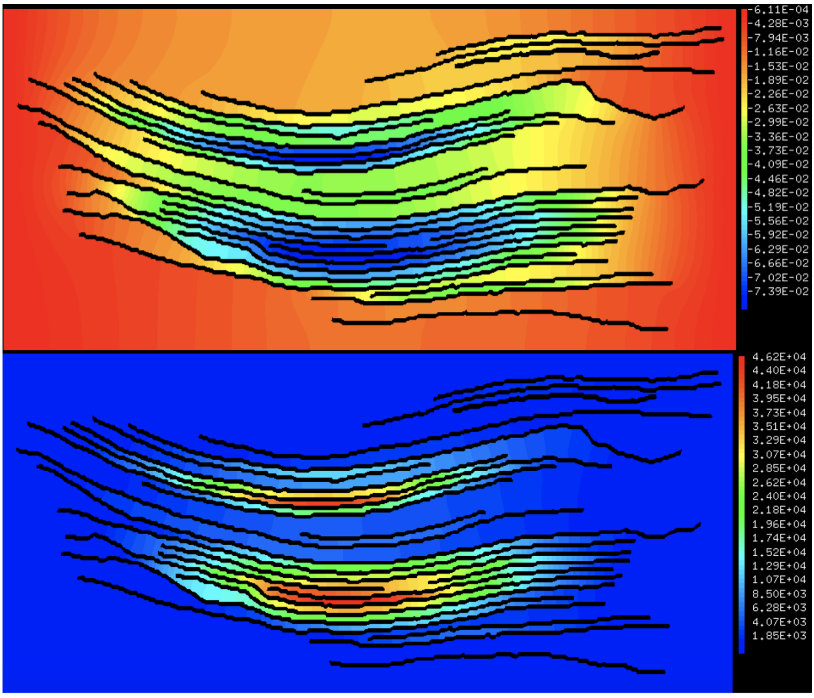

Fig. 2 Electric potential $\psi_{\text{in}}^{(0)}$ in V (above) and osmotic pressure $p_{\text{in}}^{(0)}$ in Pa as defined by Eq. (29) (below), computed with $c_{\text{ex}}^{(0)} = 1\text{mol} \cdot \text{m}^{-3}$ and $\sigma = 0.025\ \text{C} \cdot \text{m}^{-2}$.

montmorillonites.
Figure 3 illustrates the concentrations $c^{+(0)}$ of Na^+ ions and $c^{-(0)}$ of Cl^- ions obtained at the first order of approximation from Eq. (7) when electrical couplings are taken into account. $c^{+(0)}$ and $c^{-(0)}$ are expressed as follows:

$$c^{\pm(0)} = c_{\text{ex}}^{\pm(0)} \exp\left(\mp \frac{F z^{\pm} \psi_{\text{in}}^{(0)}}{RT}\right) \tag{30}$$

As expected from the assumed Boltzmann concentration distribution, cation inclusion and anion exclusion effects are clearly observed, particularly within the more densely stacked montmorillonite layers.

Figure 4 represents the evolution of the minimum value of the electric potential $\psi_{\text{in}}^{(0)}$ on the interface Γ' between the interlayer water and the montmorillonite surface when the bulk concentration $c_{\text{ex}}^{(0)}$ varies between 10^{-3} mol$\cdot$m^{-3} and 10 mol $\cdot$ m^{-3}, for a fixed value surface charge density σ (σ = 0.025, 0.045, and 0.07 C$\cdot$ m^{-2}). As expected, the electric potential in the vicinity of the montmorillonite layers' surface strongly depends on the given surface charge density σ and the bulk ionic concentration $c_{\text{ex}}^{(0)}$. As observed in (Liu et al., 2019; Smith et al., 2004), $\psi_{\text{in}}^{(0)}$ increases in the interlayer pores when

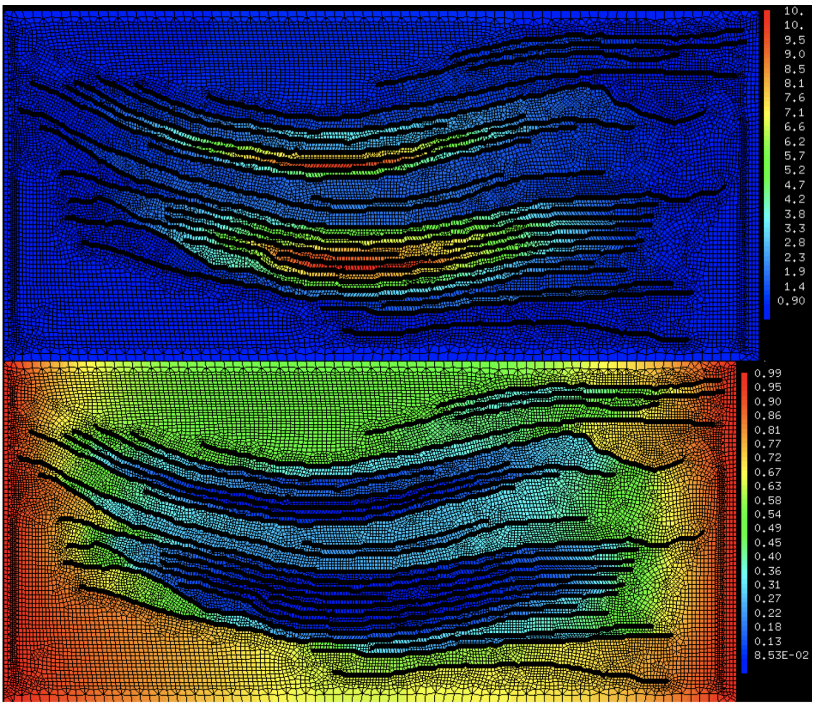

Fig. 3 Cation concentration $c^{+(0)}$ (above) and anion concentration $c^{-(0)}$ (below) in mol $\cdot$ m^{-3}, computed with $c_{\mathrm{ex}}^{(0)} = 1\mathrm{mol} \cdot \mathrm{m}^{-3}$ and $\sigma = 0.025$ C $\cdot$ m^{-2}

.

σ increases and/or the ionic concentration in the bulk solution $c_{\mathrm{ex}}^{(0)}$ decreases. These results are consistent with the fact that the electric double-layer (EDL) thickness, and hence the magnitude of the surface potential, decrease with the electrolyte concentration for a fixed value of surface charge density. As in (Liu et al., 2019; Smith et al., 2004), we observe that for a given value of $c_{\mathrm{ex}}^{(0)}$ the surface charge density σ plays a significant role in the increase of the magnitude of the electric potential, with a decaying influence of σ when $c_{\mathrm{ex}}^{(0)}$ increases.

4.2 Effective diffusion tensor

4.2.1 At the mesoscopic scale

According to Eq. (24), the cation concentration $c_{\mathrm{ex}}^{+(1)}$ at the second order of approximation is obtained by solving the problems verified by c_1^+ and c_2^+ (Annex B), which are displayed in Figure 5. c_1^+ is associated with the macroscopic electrolyte concentration gradient in the horizontal direction $\frac{\partial c_{\mathrm{ex}}^{+(0)}}{\partial x}$ and is computed by solving the system of Eqs. (B12) for $l = 1$. c_2^+ is associated with the vertical macroscopic electrolyte concentration gradient $\frac{\partial c_{\mathrm{ex}}^{+(0)}}{\partial y}$ and is computed by solving the system of Eqs. (B12) for $l = 2$. The consideration of

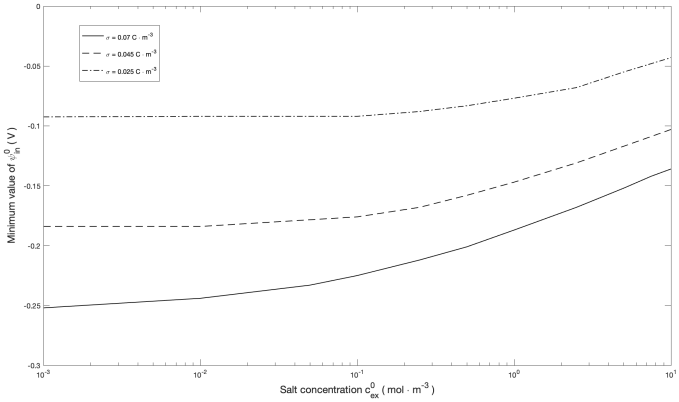

Fig. 4 Evolution of the minimum value of the electric potential $\psi_{\text{in}}^{(0)}$ with ionic concentration $c_{\text{ex}}^{(0)}$.

the local problems at the second order of approximation is necessary because c_1^+ and c_2^+ are required in order to compute the effective diffusion tensor at the mesoscopic scale $\mathcal{D}^{\pm}$ using Eq. (27). From the distribution of c_1^+, it appears that the ionic diffusion along the horizontal direction is largely unaffected in the wider interlayer spaces, as it takes place in a direction approximately parallel to the montmorillonite platelets. On the other hand, the distribution of c_2^+ clearly shows that diffusion is strongly hindered along the vertical direction by the elongated montmorillonite layers which create longer diffusion pathways. Consequently, the diffusion tensor is strongly anisotropic.
With the present microstructure $\mathcal{D}_{xx}^{+} = 1.378D^{\pm}$, $\mathcal{D}_{yy}^{+} = 0.153D^{\pm}$ for the cations, and $\mathcal{D}_{xx}^{-} = 0.435D^{\pm}$, $\mathcal{D}_{yy}^{-} = 0.123D^{\pm}$ for the anions.
A qualitative comparison can be made with experimental diffusivities obtained for various cations and anions with Na-Wyoming montmorillonite gels (Nakashima, 2003), which are comprised between $0.5D^{\pm}$ and $D^{\pm}$. In (Kemper and van Schaik, 1966; Kozaki et al., 2001) the experimental diffusivities reported for NaCl in montmorillonite are lower, and vary between $0.20D^{\pm}$ and $0.25D^{\pm}$. The numerical diffusivities computed fall within the range of the experimental values obtained under the assumption of isotropy. More details would be required about the microstructural features of the smectite clays employed in the experiments to push the comparison further.

4.2.2 At the macroscopic scale

The effective diffusion tensor $\mathcal{D}^{\pm}$ obtained at the mesoscopic scale is then used to simulate diffusion at the scale of a Wyoming bentonite sample comprising clay gels (79.7 %), solid grains (11.3 %) and micropores (9 %) (Pusch, 2001), as described in Section 2.

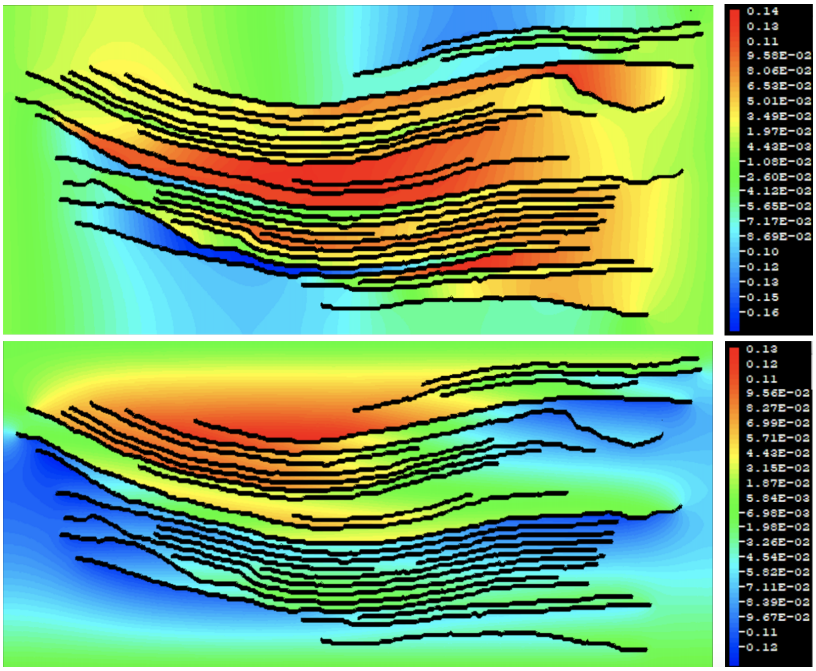

Fig. 5 Distributions of c_1^+ (above) and c_2^+ (below) in $\mathrm{mol}\cdot\mathrm{m}^{-3}$, computed with $c_{\mathrm{ex}}^{(0)} = 1\mathrm{mol}\cdot\mathrm{m}^{-3}$ and $\sigma = 0.025\ \mathrm{C}\cdot\mathrm{m}^{-2}$.

The diffusion properties of clay gels are given by the mesoscopic diffusion tensor $\mathcal{D}^{\pm}$ defined by Eq. (27) and computed in the previous section. For the micropores Ω'_v, we assume that the constant diffusion coefficient is given by the self-diffusion coefficient $D_{0,i}$ of solute i in bulk water. The solute concentration verifies the mesoscopic transport equation Eq. (26) within clay gels, and the classical diffusion equation within micropores. Both the solute concentration and diffusive fluxes are assumed to be continuous at the interface Γ'_{cv} between clay gels and micropores. A null outflow boundary condition is imposed on the interface Γ'_{cs} between clay gels and solid grains, as well as on the interface Γ'_{vs} between micropores and solid grains. An asymptotic analysis similar to that described at the mesoscopic scale is now performed at the level of the bentonite microstructure. At this scale, the small parameter $\varepsilon \ll 1$ is defined as $\varepsilon = \frac{l}{L}$, with L the macroscopic length, for instance L may represent the diameter of the bentonite sample during a diffusion test in the laboratory. For more details, we refer to (Bouchelaghem, 2018, 2022). The components $\mathcal{D}_{ik}^{\mathrm{macro}}$ of the macroscopic diffusion tensor $\mathcal{D}^{\mathrm{macro}}$ are then defined as follows $(i, j, k = 1, 2)$:

$$\mathcal{D}_{ik}^{\mathrm{macro}} = \frac{1}{|\Omega'_{\mathrm{total}}|} \int_{\Omega' \cup \Omega'_{\mathrm{v}}} a_{ij} \left(\delta_{jk} + \frac{\partial \phi_k}{\partial y_j} \right) dV \tag{31}$$

with $|\Omega'_{\mathrm{total}}| = |\Omega' + \Omega'_v + \Omega'_{\mathrm{solid}}|$ the microstructure composed of clay gels Ω' which are now viewed as a 'single' constituent after upscaling, micropores

Ω'_v and solid grains Ω'_{solid}; a_{ij} $(i,j=1,2)$ is the local diffusion tensor at the mesoscopic scale, such that $a_{ij}=\mathcal{D}_{ij}$ in clay gels Ω', $a_{ij}=D^+$ for cations and $a_{ij}=D^-$ for anions within the micropores Ω'_{v}.
To determine the components $\mathcal{D}^{\text{macro}}_{ik}$ of the macroscopic diffusion tensor, the following system has to be solved for ϕ_k $(k=1,2)$ on the quarter of the REV of side length $L_m=\frac{L}{4}$:

$$\begin{aligned}
\frac{\partial}{\partial y_i}\left(a_{ij}\frac{\partial \phi_k}{\partial y_j}\right)&=0 \text{ in } \Omega'\cup\Omega'_v,\\
\left[\left[n_i a_{ij}\frac{\partial \phi_k}{\partial y_j}\right]\right]&=-\left[[n_i a_{ik}]\right] \text{ on } \Gamma'_{cv},\\
[[\phi_k]]&=0 \text{ on } \Gamma'_{cv},\\
n_i a_{ij}\frac{\partial \phi_k}{\partial y_j}&=-n_i a_{ik} \text{ on } \Gamma'_{cs},\\
n_j\frac{\partial \phi_k}{\partial y_j}&=-n_k \text{ on } \Gamma'_{vs},\\
\mathbf{n}\cdot\nabla_y\phi_k=0 \text{ on } y_i=0 \text{ and } y_i&=\frac{Lm}{2},\ i\neq k,\\
\phi_k=0 \text{ on } y_k=0 \text{ and } y_k&=\frac{Lm}{2}
\end{aligned}$$

where the notation $[[f]]$ designates the discontinuity of any function f which takes different values $f_{|\partial\Omega_c\cap\Gamma_{cv}}$ and $f_{|\partial\Omega_v\cap\Gamma_{cv}}$ on either side of Γ_{cv} owing to the fact that the diffusion properties are different in clay gels and micropores : $[[f]]=f_{|\partial\Omega_c\cap\Gamma_{cv}}-f_{|\partial\Omega_v\cap\Gamma_{cv}}$.

Figure 6 illustrates the local fields ϕ_1 and ϕ_2 that have to be derived with respect to the mesoscopic spatial coordinates in order to obtain $\mathcal{D}^{\text{macro}}$.

The diffusion coefficients computed at the scale of montmorillonite layers are assigned to the clay gels, and their contribution is predominant for macroscopic diffusion. The components of the macroscopic diffusion tensor: $\mathcal{D}^{\text{macro}}_{xx}=4.43\times10^{-10}$ m$^2\cdot$ s^{-1}, and $\mathcal{D}^{\text{macro}}_{yy}=3.91\times10^{-10}$ m$^2\cdot$ s^{-1}, are close to experimental values reported in (Sato and Suzuki, 2003; Smith et al., 2004) for smectite clays. In the present simulation, the total porosity originating from interlayer spaces (at the level of montmorillonite layers) and micropores (in the bentonite sample) is approximately equal to 74.5 %. For the experiments reported in (Sato and Suzuki, 2003; Smith et al., 2004), no details are given regarding the distribution of porosity, while based on the values given for dry density the total porosity varies between 63 % and 76 %. As already observed in (Sato and Suzuki, 2003; Suzuki et al., 2004), there is no definite influence of the compaction level on the diffusion tensor anisotropy. This is mainly due to the presence of incompressible solid grains and large inter-particle pores which contribute to orient the diffusion pathways in all directions, thereby smearing out the anisotropy present at the scale of montmorillonite layers (Suuronen et al., 2014).

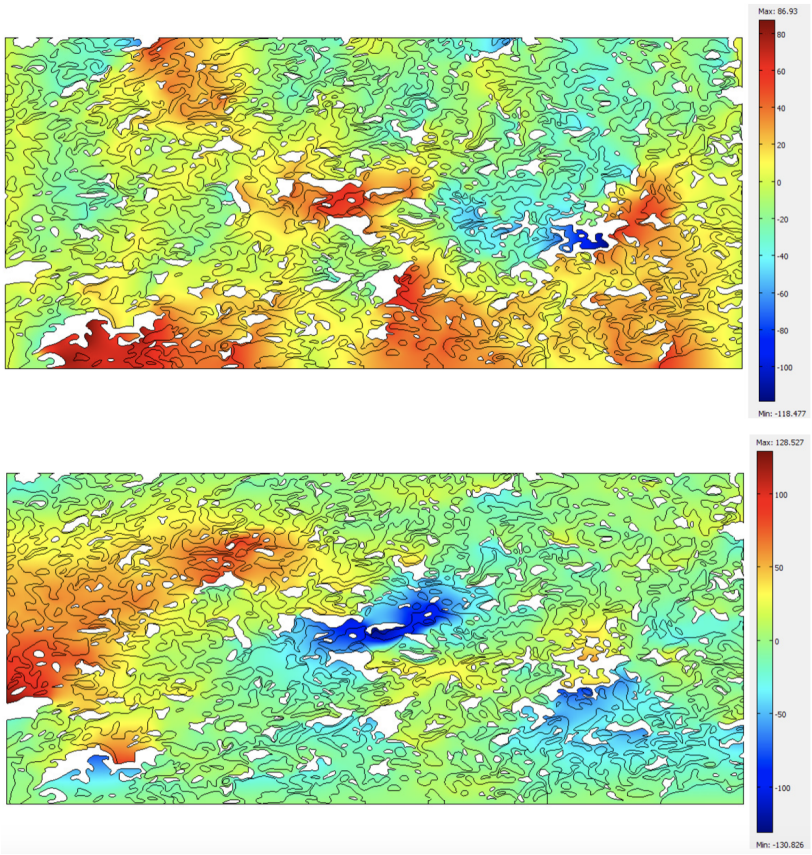

Fig. 6 Distributions of ϕ_1 (above) and ϕ_2 (below). Image width: 30μm.

5 Conclusion

A simple model has been proposed to describe ion transport by diffusion through montmorillonite, by relying on a realistic description of the interlayer space and taking into account the coupling between diffusion and electrostatic effects. Local electric potential and ion concentration maps have shown that the presence of an electric potential strongly affects the local ion concentration distributions in the vicinity of the montmorillonite surfaces.

Through upscaling, the transport equation written for each transported species at the mesoscopic scale of clay gels allows to define a mesoscopic diffusion tensor which strongly depends on the electric potential distribution within the interlayer pores and the morphology of the montmorillonite layers. The mesoscopic transport equation features also a coupling term depending on the induced membrane potential. At the montmorillonite scale, the model gives promising results, other microstructures are currently being tested in order to compare with existing experimental data available for single binary monovalent salts.

At the scale of clay gels, mineral grains and inter-particle pores, the microstructures need to be improved in order to be able to simulate diffusion in three-dimensional conditions. Other perspectives for the work include accounting for advection in order to compute the hydrostatic pressure gradient $\nabla_x p_{\text{ex}}^{(0)}$ and the membrane efficiency $\frac{\nabla_x p_{\text{ex}}^{(0)}}{2\,RT\nabla_x c_{\text{ex}}^{(0)}}$ (Cheng and Hendry, 2014). Finally, even at the level of the montmorillonite layers, it would be interesting to apply the model to 3D microstructures, as recent research indicates large ranges of variation for montmorillonite particles' sizes, that imply a three-dimensional network of interconnected pores (Whittaker et al., 2020).

Appendix A Notation

Ω : microstructure of montmorillonite (in m^3)
Ω_s : solid phase of montmorillonite layers in Ω (in m^3)
Ω_f : water-saturated interstitial space in Ω (in m^3)
c_i : concentration of ions i in pore solution (in $\text{mol} \cdot \text{m}^{-3}$)
z_i : valence of ions i in pore solution (dimensionless)
$D_{0,i}$: self-diffusion coefficient of ion i in the pore fluid (in $\text{m}^2 \cdot \text{s}^{-1}$)
F : Faraday's constant (in $\text{C} \cdot \text{mol}^{-1}$)
R : universal gas constant (in $\text{J} \cdot \text{K}^{-1} \cdot \text{mol}^{-1}$)
T : absolute temperature (in K)
∇_x : nabla operator of differentiation with respect to x
x : Cartesian spatial coordinates at the mesoscopic scale (in m)
ψ : electric potential (in V)
$\tilde{\epsilon}$: permittivity (in $\text{C}^2 \cdot \text{J}^{-1} \cdot \text{m}^{-1}$)
ϵ_0 : permittivity of vacuum (in $\text{C}^2 \cdot \text{J}^{-1} \cdot \text{m}^{-1}$)
ϵ_w : relative permittivity of water (dimensionless)
Γ : montmorillonite platelets' surface (in m^2)
$\mathbf{n}$: normal unit vector on Γ
σ: surface charge density (in $\text{C} \cdot \text{m}^{-2}$)
c^+: cations concentration of valence z^+ in binary solution (in $\text{mol} \cdot \text{m}^{-3}$)
c^-: anions concentration of valence z^- in binary solution (in $\text{mol} \cdot \text{m}^{-3}$)
D^+: self-diffusion coefficients for cations (in $\text{m}^2 \cdot \text{s}^{-1}$)
D^-: self-diffusion coefficients for anions (in $\text{m}^2 \cdot \text{s}^{-1}$)
ψ_{ex}: contribution to the electric potential ψ due to the exterior solution (in V)
ψ_{in}: contribution to the electric potential ψ due the interior diffuse double layer (DDL) (in V)
c_{ex}^+: cation concentration in the exterior solution surrounding the montmorillonite layers (in $\text{mol} \cdot \text{m}^{-3}$)
c_{ex}^-: anion concentration in the exterior solution surrounding the montmorillonite layers (in $\text{mol} \cdot \text{m}^{-3}$)
l': microscopic length associated with heterogeneities present within the microstructure (in m)
l: mesoscopic length associated with the characteristic dimension of a montmorillonite particle (in m)

τ_{D}: Debye length (in m)
ε': small perturbation parameter (dimensionless)
y : Cartesian spatial coordinates at the local scale within the microstructure (in m)
y'_i: dimensionless space variable at the microscopic scale (in m)
x'_i: dimensionless space variable at the mesoscopic scale (in m)
Ω' : dimensionless volume of montmorillonite at the microscopic scale
Ω'_{f} : dimensionless volume of interstitial space at the microscopic scale
Ω'_{s} : dimensionless volume of montmorillonite layers at the microscopic scale
Γ': dimensionless interface between the montmorillonite layers and the interstitial space
$\beta_l(y)$ $(l = 1, 2)$: coefficients expressing the variation of the electric potential within the interstitial space Ω'_{f}
$c_l^{\pm}(y)$ $(l = 1, 2)$: coefficients expressing the variation of the electrolyte concentration (+: cations, −: anions) within Ω'_{f} under the effect of a mesoscopic concentration gradient (dimensionless)
$d_l^{\pm}(y)$ $(l = 1, 2)$: coefficients expressing the variation of the electrolyte concentration (+ for cations, − for anions) within Ω'_{f} under the effect of the induced membrane potential gradient (dimensionless)
$\mathcal{D}^{\pm}$: mesoscopic diffusion tensors (+ for cations, − for anions) (in $\mathrm{m}^2 \cdot \mathrm{s}^{-1}$)
$\mathcal{D}_{\psi}^{\pm}$: mesoscopic coupling tensors (+ for cations, − for anions) (in $\mathrm{m}^2 \cdot \mathrm{s}^{-1}$)
$p_{\mathrm{in}}^{(0)}$: osmotic pressure within the interstitial space (in Pa)
Ω'_{total} : microstructure of bentonite (dimensionless)
Ω': clay gels (hydrated montmorillonite particles) present in Ω'_{total} (dimensionless)
Ω'_v: micropores present in Ω'_{total} (dimensionless)
Ω'_{solid}: solid grains present in Ω'_{total} (dimensionless)
Γ'_{cv}: interface between clay gels and micropores (dimensionless)
Γ'_{cs}: interface between clay gels and solid grains (dimensionless)
Γ'_{vs}: interface between micropores and solid grains (dimensionless)
ε: small perturbation parameter
L: macroscopic length of the bentonite sample (in m)
$\mathcal{D}^{\mathrm{macro}}$: macroscopic diffusion tensor (in $\mathrm{m}^2 \cdot \mathrm{s}^{-1}$)

Appendix B Development of the local problems

Taking Eq. (12) at order $\mathcal{O}((\varepsilon')^{-2})$ and Eq. (16) at order $\mathcal{O}((\varepsilon')^0) = \mathcal{O}(1)$, we have, using Einstein summation convention on repeated indices:

$$\frac{\partial}{\partial y_i}\left(\frac{\partial \psi_{\mathrm{ex}}^{(0)}}{\partial y_i}\right) = 0 \text{ in } \Omega'_{\mathrm{f}},$$

$$\frac{\partial \psi_{\mathrm{ex}}^{(0)}}{\partial y_i} n_i = \nabla_y \psi_{\mathrm{ex}}^{(0)} \cdot \mathbf{n} = 0 \text{ on } \Gamma'$$

Multiplying the equation above by $\psi_{\mathrm{ex}}^{(0)}$ and integrating by parts in Ω'_{f} while accounting for the associated boundary condition on Γ', the Ω'-periodicity of $\frac{\partial \psi_{\mathrm{ex}}^{(0)}}{\partial y_i}$ and the Ω'-antiperiodicity of the normal vector $\mathbf{n}$, we obtain that $\frac{\partial \psi_{\mathrm{ex}}^{(0)}}{\partial y_i} = 0$ in Ω'_{f} and therefore $\psi_{\mathrm{ex}}^{(0)} = \psi_{\mathrm{ex}}^{(0)}(x_i)$.
Taking Eq. (12) at the order $\mathcal{O}((\varepsilon')^{-1})$ and Eq. (16) at the order $\mathcal{O}(\varepsilon')$, we have:

$$\frac{\partial}{\partial x_i}\left(\frac{\partial \psi_{\mathrm{ex}}^{(0)}}{\partial y_i}\right) + \frac{\partial}{\partial y_i}\left(\frac{\partial \psi_{\mathrm{ex}}^{(0)}}{\partial x_i} + \frac{\partial \psi_{\mathrm{ex}}^{(1)}}{\partial y_i}\right) = 0 \text{ in } \Omega'_{\mathrm{f}},$$

$$\left(\frac{\partial \psi_{\mathrm{ex}}^{(1)}}{\partial y_i} + \frac{\partial \psi_{\mathrm{ex}}^{(0)}}{\partial x_i}\right) n_i = 0 \text{ on } \Gamma'$$

Since $\psi_{\mathrm{ex}}^{(0)} = \psi_{\mathrm{ex}}^{(0)}(x_i)$, the previous system can be simplified as follows:

$$\frac{\partial}{\partial y_i}\left(\frac{\partial \psi_{\mathrm{ex}}^{(1)}}{\partial y_i}\right) = \Delta_y \psi_{\mathrm{ex}}^{(1)} = 0 \text{ in } \Omega'_{\mathrm{f}},$$

$$\frac{\partial \psi_{\mathrm{ex}}^{(1)}}{\partial y_i} n_i = -\frac{d\psi_{\mathrm{ex}}^{(0)}}{dx_i} n_i \text{ on } \Gamma'$$

implying that $\psi_{\mathrm{ex}}^{(1)}$ depends linearly on $\frac{\partial \psi_{\mathrm{ex}}^{(0)}}{\partial x_i}$. We can therefore introduce two functions that depend only on y_i, $\beta_l(y)$ for $l = 1, 2$ in 2D, such that:

$$\psi_{\mathrm{ex}}^{(1)} = \beta_l(y) \frac{d\psi_{\mathrm{ex}}^{(0)}(x)}{dx_l} = \boldsymbol{\beta}(y) \cdot \nabla_x \psi_{\mathrm{ex}}^{(0)} \tag{B1}$$

and, by inserting Eq. (B1) in the system verified by $\psi_{\mathrm{ex}}^{(1)}$, we have:

$$\Delta_y \beta_l = 0 \text{ in } \Omega'_{\mathrm{f}}, \tag{B2}$$

$$\frac{\partial \beta_l}{\partial y_i} n_i = \nabla_y \beta_l \cdot \mathbf{n} = -n_l \text{ on } \Gamma' \text{ , l = 1,2} \tag{B3}$$

$$\beta_l \ \Omega'\text{-periodical} \tag{B4}$$

$$\langle \beta_l \rangle = \frac{1}{|\Omega'|} \int_{\Omega'_{\mathrm{f}}} \beta_l dV = 0 \tag{B5}$$

By taking Eq. (10) at order $\mathcal{O}((\varepsilon')^{-2})$ and Eq. (14) at order $\mathcal{O}((\varepsilon')^{-1})$, we have:

$$\frac{\partial}{\partial y_i}\left(D'^{+} \exp\left(-z^{+}\psi_{\mathrm{in}}^{(0)}\right)\left(\frac{\partial c_{\mathrm{ex}}^{+(0)}}{\partial y_i} + z^{+} c_{\mathrm{ex}}^{+(0)} \frac{\partial \psi_{\mathrm{ex}}^{(0)}}{\partial y_i}\right)\right) = 0 \text{ in } \Omega'_{\mathrm{f}}$$

$$D^{+}\exp\left(-z^{+}\psi_{\mathrm{in}}^{(0)}\right)\left(\frac{\partial c_{\mathrm{ex}}^{+(0)}}{\partial y_i}+z^{+}c_{\mathrm{ex}}^{+(0)}\frac{\partial \psi_{\mathrm{ex}}^{(0)}}{\partial y_i}\right)n_i=0 \text{ on } \Gamma'$$

As $\psi_{\mathrm{ex}}^{(0)}=\psi_{\mathrm{ex}}^{(0)}(x_i)$ does not depend on y_i, we obtain simply:

$$\frac{\partial}{\partial y_i}\left(D^{+}\exp\left(-z^{+}\psi_{\mathrm{in}}^{(0)}\right)\frac{\partial c_{\mathrm{ex}}^{+(0)}}{\partial y_i}\right)=0 \text{ in } \Omega_{\mathrm{f}}'$$

$$D^{+}\exp\left(-z^{+}\psi_{\mathrm{in}}^{(0)}\right)\frac{\partial c_{\mathrm{ex}}^{+(0)}}{\partial y_i}\,n_i=0 \text{ on } \Gamma'$$

Multiplying the equation above by $c_{\mathrm{ex}}^{+(0)}$ and integrating by parts in Ω_{f}' while accounting for the boundary condition on Γ', the Ω'-periodicity of $\frac{\partial c_{\mathrm{ex}}^{+(0)}}{\partial y_i}$ and the Ω'-antiperiodicity of the normal vector $\mathbf{n}$, we obtain that $\frac{\partial c_{\mathrm{ex}}^{+(0)}}{\partial y_i}=0$ and therefore $c_{\mathrm{ex}}^{+(0)}=c_{\mathrm{ex}}^{+(0)}(x_i)$.
Similarly, Eq. (11) at order $\mathcal{O}((\varepsilon')^{-2})$ and Eq. (15) at order $\mathcal{O}((\varepsilon')^{-1})$ lead to $c_{\mathrm{ex}}^{-(0)}=c_{\mathrm{ex}}^{-(0)}(x_i)$.
Taking Eq. (10) at order $\mathcal{O}((\varepsilon')^{-1})$ and Eq. (14) at order $\mathcal{O}(1)$, and taking into account that $\psi_{\mathrm{ex}}^{(0)}=\psi_{\mathrm{ex}}^{(0)}(x_i)$ and $c_{\mathrm{ex}}^{+(0)}=c_{\mathrm{ex}}^{+(0)}(x_i)$, we can write:

$$\frac{\partial}{\partial y_i}\left(D'^{+}\exp\left(-z^{+}\psi_{\mathrm{in}}^{(0)}\right)\left(\frac{\partial c_{\mathrm{ex}}^{+(1)}}{\partial y_i}+\frac{\partial c_{\mathrm{ex}}^{+(0)}}{\partial x_i}+z^{+}c_{\mathrm{ex}}^{+(0)}\left(\frac{\partial \psi_{\mathrm{ex}}^{(1)}}{\partial y_i}+\frac{\partial \psi_{\mathrm{ex}}^{(0)}}{\partial x_i}\right)\right)\right)=0 \text{ in } \Omega_{\mathrm{f}}' \tag{B6}$$

$$D'^{+}\exp\left(-z^{+}\psi_{\mathrm{in}}^{(0)}\right)\left(\frac{\partial c_{\mathrm{ex}}^{+(1)}}{\partial y_i}+\frac{\partial c_{\mathrm{ex}}^{+(0)}}{\partial x_i}+z^{+}c_{\mathrm{ex}}^{+(0)}\left(\frac{\partial \psi_{\mathrm{ex}}^{(1)}}{\partial y_i}+\frac{\partial \psi_{\mathrm{ex}}^{(0)}}{\partial x_i}\right)\right)n_i=0 \text{ on } \Gamma' \tag{B7}$$

According to Eq. (B1), $\psi_{\mathrm{ex}}^{(0)}$ is a linear function of $\frac{d\psi_{\mathrm{ex}}^{(0)}}{dx_i}$, and therefore the system of equations written for $c_{\mathrm{ex}}^{+(1)}$ is linear with respect to the mesoscopic potential gradient $\frac{\partial \psi_{\mathrm{ex}}^{(0)}}{\partial x_i}$ and the mesoscopic concentration gradient $\frac{\partial c_{\mathrm{ex}}^{+(0)}}{\partial x_i}$. The boundary condition on Γ' clearly shows that the source for the spatial evolution of $c_{\mathrm{ex}}^{+(1)}$ is $\frac{\partial c_{\mathrm{ex}}^{+(0)}}{\partial x_i}$ and $\frac{\partial \psi_{\mathrm{ex}}^{(0)}}{\partial x_i}$, and we can assume:

$$c_{\mathrm{ex}}^{+(1)}(x,y)=c_l^{+}(y)\,\frac{\partial c_{\mathrm{ex}}^{+(0)}}{\partial x_l}(x)+d_l^{+}(y)\,z^{+}c_{\mathrm{ex}}^{+(0)}\,\frac{\partial \psi_{\mathrm{ex}}^{(0)}}{\partial x_l}(x) \tag{B8}$$

with c_l^{+} and d_l^{+}, $l=1,2$, Ω'-periodic characteristic functions. Similarly, from Eq. (11) at the order $\mathcal{O}((\varepsilon')^{-1})$ and Eq. (15) at the order $\mathcal{O}(1)$ and the same approach, we have:

$$\frac{\partial}{\partial y_i}\left(D'^{-}\exp\left(z^{-}\psi_{\mathrm{in}}^{(0)}\right)\left(\frac{\partial c_{\mathrm{ex}}^{-(1)}}{\partial y_i}+\frac{\partial c_{\mathrm{ex}}^{-(0)}}{\partial x_i}-z^{-}c_{\mathrm{ex}}^{-(0)}\left(\frac{\partial \psi_{\mathrm{ex}}^{(1)}}{\partial y_i}+\frac{\partial \psi_{\mathrm{ex}}^{(0)}}{\partial x_i}\right)\right)\right)=0 \text{ in } \Omega_{\mathrm{f}}' \tag{B9}$$

$$D'^{-}\exp\left(z^{-}\psi_{\text{in}}^{(0)}\right)\left(\frac{\partial c_{\text{ex}}^{-(1)}}{\partial y_i}+\frac{\partial c_{\text{ex}}^{-(0)}}{\partial x_i}-z^{-}c_{\text{ex}}^{-(0)}\left(\frac{\partial \psi_{\text{ex}}^{(1)}}{\partial y_i}+\frac{\partial \psi_{\text{ex}}^{(0)}}{\partial x_i}\right)\right)n_i=0 \text{ on } \Gamma' \tag{B10}$$

leading to:

$$c_{\text{ex}}^{-(1)}(x,y)=c_l^{-}(y)\,\frac{\partial c_{\text{ex}}^{-(0)}}{\partial x_l}(x)-d_l^{-}(y)\,z^{-}c_{\text{ex}}^{-(0)}\,\frac{\partial \psi_{\text{ex}}^{(0)}}{\partial x_l}(x) \tag{B11}$$

with c_l^{-} and d_l^{-}, $l=1,2$, Ω'-periodic characteristic functions.
The systems verified by $c_l^{\pm}$ and $d_l^{\pm}$ ($l=1,2$) are obtained by inserting Eq. (B8) into Eqs. (B6) and (B7) for c_l^{+} and d_l^{+}, and by inserting Eq. (B11) into Eqs. (B9) and (B10) for c_l^{-} and d_l^{-}:

$$\begin{aligned}
\frac{\partial}{\partial y_i}\left(D^{\pm}\exp\left(\mp z^{\pm}\psi_{\text{in}}^{(0)}\right)\left(\frac{\partial c_l^{\pm}}{\partial y_i}+\delta_{il}\right)\right)&=0 \text{ in } \Omega'_{\text{f}},\\
D^{\pm}\exp\left(\mp z^{\pm}\psi_{\text{in}}^{(0)}\right)\left(\frac{\partial c_l^{\pm}}{\partial y_i}+\delta_{il}\right)n_i&=0 \text{ on } \Gamma',\\
c_l^{\pm}\ &\ \Omega'\text{-periodical}\\
\langle c_l^{\pm}\rangle=\frac{1}{|\Omega'|}\int_{\Omega'_{\text{f}}}c_l^{\pm}dV&=0
\end{aligned} \tag{B12}$$

$$\begin{aligned}
\frac{\partial}{\partial y_i}\left(D^{\pm}\exp\left(\mp z^{\pm}\psi_{\text{in}}^{(0)}\right)\left(\frac{\partial d_l^{\pm}}{\partial y_i}+\frac{\partial \beta_l}{\partial y_i}+\delta_{il}\right)\right)&=0 \text{ in } \Omega'_{\text{f}},\\
D^{\pm}\exp\left(\mp z^{\pm}\psi_{\text{in}}^{(0)}\right)\left(\frac{\partial d_l^{\pm}}{\partial y_i}+\frac{\partial \beta_l}{\partial y_i}+\delta_{il}\right)n_i&=0 \text{ on } \Gamma',\\
d_l^{\pm}\ &\ \Omega'\text{-periodical}\\
\langle d_l^{\pm}\rangle=\frac{1}{|\Omega'|}\int_{\Omega'_{\text{f}}}d_l^{\pm}dV&=0
\end{aligned} \tag{B13}$$

Appendix C Effective tensors at the mesoscopic scale

We now write Eqs. (10) and (11) at order $\mathcal{O}((\varepsilon')^0)=\mathcal{O}(1)$. By taking into account the results obtained in Appendix (B), $\psi_{\text{ex}}^{(0)}=\psi_{\text{ex}}^{(0)}(x_i)$ and $c_{\text{ex}}^{+(0)}=c_{\text{ex}}^{+(0)}(x_i)$, we have:

$$\begin{aligned}
&\frac{\partial}{\partial y_i}\left(D^{\pm}\exp\left(\mp z^{\pm}\psi_{\text{in}}^{(0)}\right)\left(\frac{\partial c_{\text{ex}}^{\pm(2)}}{\partial y_i}+\frac{\partial c_{\text{ex}}^{\pm(1)}}{\partial x_i}\right)\right)\\
+&\frac{\partial}{\partial y_i}\left(D^{\pm}\exp\left(\mp z^{\pm}\psi_{\text{in}}^{(0)}\right)(\pm z^{\pm})\left(c_{\text{ex}}^{\pm(0)}\frac{\partial \psi_{\text{ex}}^{(2)}}{\partial y_i}+c_{\text{ex}}^{\pm(1)}\frac{\partial \psi_{\text{ex}}^{(1)}}{\partial y_i}\right)\right)
\end{aligned}$$

$$+\frac{\partial}{\partial y_i}\left(D^{\pm}\exp\left(\mp z^{\pm}\psi_{\text{in}}^{(0)}\right)(\pm z^{\pm})\left(c_{\text{ex}}^{\pm(0)}\frac{\partial\psi_{\text{ex}}^{(1)}}{\partial x_i}+c_{\text{ex}}^{\pm(1)}\frac{\partial\psi_{\text{ex}}^{(0)}}{\partial x_i}\right)\right)$$

$$+\frac{\partial}{\partial y_i}\left(D^{\pm}\exp\left(\mp z^{\pm}\psi_{\text{in}}^{(0)}\right)(\mp z^{\pm})\psi_{\text{in}}^{(1)}\left(\frac{\partial c_{\text{ex}}^{\pm(1)}}{\partial y_i}+\frac{\partial c_{\text{ex}}^{\pm(0)}}{\partial x_i}\right)\right) \quad \text{(C14)}$$

$$-\frac{\partial}{\partial y_i}\left(D^{\pm}\exp\left(\mp z^{\pm}\psi_{\text{in}}^{(0)}\right)(z^{\pm})^2\psi_{\text{in}}^{(1)}\left(c_{\text{ex}}^{\pm(0)}\frac{\partial\psi_{\text{ex}}^{(1)}}{\partial y_i}+c_{\text{ex}}^{\pm(0)}\frac{\partial\psi_{\text{ex}}^{(0)}}{\partial x_i}\right)\right)$$

$$+\frac{\partial}{\partial x_i}\left(D^{\pm}\exp\left(\mp z^{\pm}\psi_{\text{in}}^{(0)}\right)\left(\frac{\partial c_{\text{ex}}^{\pm(1)}}{\partial y_i}+\frac{\partial c_{\text{ex}}^{\pm(0)}}{\partial x_i}\right)\right)$$

$$+\frac{\partial}{\partial x_i}\left(D^{\pm}\exp\left(\mp z^{\pm}\psi_{\text{in}}^{(0)}\right)(\pm z^{\pm})\left(c_{\text{ex}}^{\pm(0)}\frac{\partial\psi_{\text{ex}}^{(1)}}{\partial y_i}+c_{\text{ex}}^{\pm(0)}\frac{\partial\psi_{\text{ex}}^{(0)}}{\partial x_i}\right)\right)=0 \text{ in } \Omega_{\text{f}}'$$

The associated boundary conditions are obtained by considering Eqs. (14) and (15) at orders $\mathcal{O}(1)$ and $\mathcal{O}(\varepsilon')$:

$$D^{\pm}\exp\left(\mp z^{\pm}\psi_{\text{in}}^{(0)}\right)\left(\frac{\partial c_{\text{ex}}^{\pm(1)}}{\partial y_i}+\frac{\partial c_{\text{ex}}^{\pm(0)}}{\partial x_i}\pm z^{\pm}c_{\text{ex}}^{\pm(0)}\left(\frac{\partial\psi_{\text{ex}}^{(1)}}{\partial y_i}+\frac{\partial\psi_{\text{ex}}^{(0)}}{\partial x_i}\right)\right)n_i=0 \text{ on } \Gamma' \quad \text{(C15)}$$

$$D^{\pm}\exp\left(\mp z^{\pm}\psi_{\text{in}}^{(0)}\right)\left(\frac{\partial c_{\text{ex}}^{\pm(2)}}{\partial y_i}+\frac{\partial c_{\text{ex}}^{\pm(1)}}{\partial x_i}\pm z^{\pm}\left(c_{\text{ex}}^{\pm(0)}\frac{\partial\psi_{\text{ex}}^{(2)}}{\partial y_i}+c_{\text{ex}}^{\pm(1)}\frac{\partial\psi_{\text{ex}}^{(1)}}{\partial y_i}\right)\right)n_i$$

$$+D^{\pm}\exp\left(\mp z^{\pm}\psi_{\text{in}}^{(0)}\right)(\pm z^{\pm})\left(c_{\text{ex}}^{\pm(0)}\frac{\partial\psi_{\text{ex}}^{(1)}}{\partial x_i}+c_{\text{ex}}^{\pm(1)}\frac{\partial\psi_{\text{ex}}^{(0)}}{\partial x_i}\right)n_i=0 \text{ on } \Gamma' \quad \text{(C16)}$$

Eq. (C14) is integrated in Ω_{f}'. Using Green's theorem, the Ω'-periodicity of the physical variables and the Ω'-antiperiodicity of the outward normal vector $\mathbf{n}$ on Γ', and boundary conditions (C15) and (C16), all the derivatives with respect to y_i disappear. And we have:

$$\int_{\Omega_{\text{f}}'}\frac{\partial}{\partial x_i}\left(D^{\pm}\exp\left(\mp z^{\pm}\psi_{\text{in}}^{(0)}\right)\left(\frac{\partial c_{\text{ex}}^{\pm(1)}}{\partial y_i}+\frac{\partial c_{\text{ex}}^{\pm(0)}}{\partial x_i}\right)\right)dV$$

$$+\int_{\Omega_{\text{f}}'}\frac{\partial}{\partial x_i}\left(D^{\pm}\exp\left(\mp z^{\pm}\psi_{\text{in}}^{(0)}\right)(\pm z^{\pm})\left(c_{\text{ex}}^{\pm(0)}\frac{\partial\psi_{\text{ex}}^{(1)}}{\partial y_i}+c_{\text{ex}}^{\pm(0)}\frac{\partial\psi_{\text{ex}}^{(0)}}{\partial x_i}\right)\right)dV=0$$

By accounting for Eqs. (B1), (B8) and (B11), we finally obtain the following expression for the mesoscopic solute transport equations (+ for cations, − for

anions):

$$\frac{\partial}{\partial x_i}\left(\int_{\Omega'_{\mathrm{f}}} D^{\pm}\exp\left(\mp z^{\pm}\psi_{\mathrm{in}}^{(0)}\right)\left(\frac{\partial c_l^{\pm}}{\partial y_i}+\delta_{li}\right)dV\,\frac{\partial c_{\mathrm{ex}}^{\pm(0)}}{\partial x_l}\right)+$$

$$\frac{\partial}{\partial x_i}\left(\int_{\Omega'_{\mathrm{f}}} D^{\pm}\exp\left(\mp z^{\pm}\psi_{\mathrm{in}}^{(0)}\right)(\pm z^{\pm})\left(\frac{\partial d_l^{\pm}}{\partial y_i}+\frac{\partial \beta_l}{\partial y_i}+\delta_{li}\right)dV\,c_{\mathrm{ex}}^{\pm(0)}\frac{\partial \psi_{\mathrm{ex}}^{(0)}}{\partial x_l}\right)=0$$

References

Bacle, P., J. Dufreche, B. Rotenberg, I. Bourg, and V. Marry. 2016. Modeling the transport of water and ionic tracers in a micrometric clay sample. *Appl Clay Sc* 123: 18–28. https://doi.org/10.1016/j.clay.2015.12.014 .

Bouchelaghem, F. 2018. Multi-scale study of pollutant transport and uptake in compacted bentonite. *Mathematical Geosciences 50*(5): 495–523. https://doi.org/10.1007/s11004-017-9724-8 .

Bouchelaghem, F. 2022. Diffusion calculations on reconstructed bentonite microstructures. Paper presented at the 4^{th} Euro-Mediterranean Conference for Environmental Integration, Sousse, Tunisia, 1–4 November 2022.

Bouchelaghem, F. and R. Pusch. 2017. Fluid flow and effective conductivity calculations on numerical images of bentonite microstructure. *Appl Clay Sc* 144: 9–18. https://doi.org/10.1016/j.clay.2017.04.023 .

Chang, F., N. Skipper, and G. Sposito. 1995. Computer simulation of interlayer molecular structure in sodium montmorillonite hydrates. *Langmuir* 11: 2734–2741. https://doi.org/10.1021/la00007a064 .

Cheng, G. and M. Hendry. 2014. Chemico-osmosis in geologic membranes: Role of membrane potential gradient. *Geochimica and Cosmochimica Acta* 141: 270–280. https://doi.org/10.1016/j.gca.2014.06.017 .

Choi, J. and D. Oscarson. 1996. Diffusive transport through compacted na- and ca-bentonite. *J Contam Hydrol* 22: 189–202. https://doi.org/10.1016/0169-7722(95)00081-X .

Glaus, M., B. Baeyens, M. Bradbury, A. Jakob, L. Van Loon, and A. Yaroschchuk. 2007. Diffusion of ^{22}na and ^{85}sr in montmorillonite: evidence of interlayer diffusion being the dominant pathway at high compaction. *Environ Sci Technol* 41: 478–485. https://doi.org/10.1021/es061908d .

Gonzales Sanchez, F., T. Gimmi, F. Juranyi, L. Van Loon, and L. Diamond. 2009. Linking the diffusion of water in compacted clays at two different time

scales: tracer through-diffusion and quasielastic neutron scattering. *Environ Sc Technol* 43: 3487–3493. https://doi.org/10.1021/es8035362 .

Gonzalez, R., R. Woods, and S. Eddins. 2004. *Digital Image Processing Using MATLAB*. New Jersey: Pearson Prentice Hall.

Gross, R.J. and J.F. Osterle. 1968. Membrane transport characteristics of ultrafine capillaries. *J Chem Phys* 49: 228–234. https://doi.org/10.1063/1.1669814 .

Hetzel, F., D. Tessier, A. Jaunet, and H. Doner. 1994. The microstructure of three na+ smectites: the importance of particle geometry on dehydration and rehydration. *Clays and Clay Minerals 42*(3): 242–248. https://doi.org/10.1346/CCMN.1994.0420302 .

Honorio, T., L. Brochard, M. Vandamme, and A. Lebee. 2018. Flexibility of nanolayers and stacks: implications in the nanostructuration of clays. *Clays and Clay Minerals* 14: 7354–7367. https://doi.org/10.1039/c8sm01359d .

Kapur, J., P. Sahoo, and A. Wong. 1985. A new method for gray-level picture thresholding using the entropy of the histogram. *Computer Vision, Graphics and Image Processing* 29: 273–285. https://doi.org/10.1016/0734-189X(85)90125-2 .

Keller, L., A. Seiphoori, P. Gasser, F. Lucas, L. Holzer, and A. Ferrari. 2014. The pore structure of compacted and partly saturated mx-80 bentonite at different dry densities. *Clays and Clay Minerals 62*(3): 174–187. https://doi.org/10.1346/CCMN.2014.0620302 .

Kemper, W. and J. van Schaik. 1966. Diffusion of salts in clay–water systems. *Soil Sci. Soc. Am. Proc* 30: 534–540. https://doi.org/10.2136/sssaj1966.03615995003000050006x .

Kozaki, T., K. Inada, S. Sato, and H. Ohashi. 2001. Diffusion mechanism of chloride ions in sodium montmorillonite. *J Contam Hydrol* 47: 159–170. https://doi.org/10.1016/S0169-7722(00)00146-7 .

Le Fichoux, B., 2022. Présentation et utilisation de cast3m, 22.0. CEA Saclay DEN/DANS/DM2S/SEMT.

Liu, X., R. Tian, W. Du, R. Li, W. Ding, and H. Li. 2019. A theory to determine the surface potentials of clay particles in electrolyte solutions. *Appl Clay Sc* 169: 112–119. https://doi.org/10.1016/j.clay.2018.12.022 .

Malikova, N., S. Longeville, J. Zanotti, E. Dubois, V. Marry, P. Turq, and J. Ollivier. 2008. Signature of low-dimensional diffusion in complex systems. *Phys Rev Letters PRL* 101: 265901. https://doi.org/10.1103/PhysRevLett.

101.265901 .

Marry, V. and P. Turq. 2003. Microscopic simulations of interlayer structure and dynamics in bihydrated heteroionic montmorillonites. *J Phys Chem B* 107: 1832–1839. https://doi.org/10.1021/jp022084z .

Morrison, F.A. and J.F. Osterle. 1965. Electrokinetic energy conversion in ultrafine capillaries. *J Chem Phys* 43: 2111–2115. https://doi.org/10.1063/1.1697081 .

Moyne, C. and M. Murad. 2006. A two-scale model for coupled electro-chemo-mechanical phenomena and onsager's reciprocity relations in expansive clays: I. homogenization analysis. *Transp Porous Media* 62: 333–380. https://doi.org/10.1007/s11242-005-1290-8 .

Nakashima, Y. 2003. Diffusivity measurement of heavy ions in wyoming montmorillonite gels by x-ray computed tomography. *J Contaminant Hydrology* 61: 147–156. https://doi.org/10.1016/S0169-7722(02)00138-9 .

Pusch, R. 2001. *The microstructure of MX-80 clay with respect to its bulk physical properties under different environmental conditions. Technical Report TR-01-08.* Stockholm, Sweden: Swedish Nuclear Fuel and Waste Management.

Sanchez-Palencia, E. 1980. Chapter 7: Fluid flow in porous media, In *Non-Homogeneous Media and Vibration Theory*, eds. Broy, M. and E. Denert, 129–157. New York: Lecture Notes in Physics 127.

Sasidhar, V. and E. Ruckenstein. 2003. Electrolyte osmosis through capillaries. *J Colloid Interface Sc* 61: 147–156. https://doi.org/10.1016/S0169-7722(02)00138-9 .

Sato, H. 2005. Effects of the orientation of smectite particles and ionic strength on diffusion and activation enthalpies of i^- and c_s^+ ions in compacted smectite. *Appl Clay Sc* 29: 267–281. https://doi.org/10.1016/j.clay.2005.02.003 .

Sato, H. and S. Suzuki. 2003. Fundamental study on the effect of an orientation of clay particles on diffusion pathway in compacted bentonite. *Appl Clay Sc* 23: 51–60. https://doi.org/10.1016/S0169-1317(03)00086-3 .

Smith, D., P. Pivonka, C. Jungnickel, and S. Fityus. 2004. Theoretical analysis of anion exclusion and diffusive transport through platy-clay soils. *Transp Porous Media* 57: 251–277. https://doi.org/10.1007/s11242-003-4056-1 .

Suuronen, J., M. Matusewicz, M. Olin, and R. Serimaa. 2014. X-ray studies on the nano- and microscale anisotropy in compacted clays: comparison of

bentonite and purified montmorillonite. *Appl Clay Sc* 101: 401–408. https://doi.org/10.1016/j.clay.2014.08.015 .

Suzuki, S., H. Sato, T. Ishidera, and N. Fujii. 2004. Study on anisotropy of effective diffusion coefficients and activation energy for deuterated water in compacted sodium bentonite. *J Contam Hydrology* 68: 23–37. https://doi.org/10.1016/S0169-7722(03)00139-6 .

Tomioka, S., T. Kozaki, H. Takamatsu, N. Noda, S. Nisiyama, N. Kozai, S. Suzuki, and S. Sato. 2010. Analysis of microstructural images of dry and water-saturated compacted bentonite samples observed with x-ray micro ct. *Appl Clay Sc* 47: 65–71. https://doi.org/10.1016/j.clay.2008.09.001 .

Tournassat, C., I. Bourg, M. Holmboe, G. Sposito, and C. Steefel. 2016. Molecular dynamics simulations of anion exclusion in clay interlayer nanopores. *Clays and Clay Minerals* 64(4): 374–388. https://doi.org/10.1346/CCMN.2016.0640403 .

Whittaker, M., L. Comolli, B. Gilbert, and J. Banfield. 2020. Layer size polydispersity in hydrated montmorillonite creates multiscale porosity networks. *Appl Clay Sc* 190: 105548. https://doi.org/10.1016/j.clay.2020.105548 .

Wu, T., Y. Yang, Z. Wang, Q. Shen, Y. Tong, and M. Wang. 2020. Anion diffusion in compacted clays by pore-scale simulation and experiments. *Water Resources Research* 56(11): e2019WR027037. https://doi.org/10.1029/2019WR027037 .

Declarations

- Ethical approval: Not applicable.
- Consent to Participate: Not applicable.
- Consent to Publish: All authors approved the version to be published and agree to be accountable for all aspects of the work.
- Authors' Contributions: All authors contributed to the study conception and design. Modelling work and numerical computations were performed by Fatiha Bouchelaghem. The first draft of the manuscript was written by Fatiha Bouchelaghem and all authors commented on previous versions of the manuscript. All authors read and approved the final manuscript.
- Funding: The authors declare that no funds, grants, or other support were received.
- Competing Interests: The authors have no relevant financial or non-financial interests to disclose.
- Availability of data and materials: Not applicable.